International Journal of Current Engineering and Technology
E-ISSN 2277 – 4106, P-ISSN 2347 – 5161

Available at http://inpressco.com/category/ijcet

Research Article

Investigation of Power Conversion Efficiency of Annealed LA-CR CO-Doped $BiFeO_3$ Perovskite Solar Cell

[1]Muhammad Qadeer Aslam, [2]Ameed Ul Hassan Alvi, [1]Esha Sajjad, [3]Mehran Ahmad, [4]Muhammad Farooq, [1]Noor Fatima, [2*]Seemab Hussnain

[1]Department of Physics, Government College University Faisalabad, Pakistan
[*2]Department of Physics, University of Agriculture Faisalabad, Pakistan
[3]Department of Physics, Riphah International University Lahore, Pakistan
[4]Department of Physics, Punjab University Lahore, Pakistan

Received 11 Nov 2023, Accepted 15 Feb 2024, Available online 21 Feb 2024, **Vol.14, No.1 (Jan/Feb 2024**)

Abstract

It has been noticed that energy crises all over the world is formidable problem, which need to be addressed and solved. Perovskite material is promising materials for clean energy production. In experimental study, lanthanum (La) Chromium (Cr) co-doped bismuth ferrites (BiFO3) were synthesized using sol-gel auto-combustion technique and manifold characterization techniques e.g., XRD, SEM, UV-Visible, and IV. A scanning electron microscope is used to examine morphology of sample. Creation of perovskite structure in the sample made using the sol-gel process was investigated by X-ray diffraction patterns. Result of XRD confirmed rhombohedral structure having R3c space-group. The crystalline size of synthesized nano particles exist between (11-18) nm. The agglomerated nano particles was examine by SEM analysis. The band gap of pure and doped BFO were studied by UV-visible spectroscopy. The ultraviolet visible absorption spectra were used to show that La-Cr co-doped was increase light absorption rate of film and decrease optical band gap. The decreased band gap can make easier the transport of carriers. Electrical properties were studied through four probe method and showed good conductivity increased by La-Cr with co-doping in the BiFeO3. The aim of this study is to gain high power conversion efficiency, narrow band gap, high remnant polarization and photovoltaic effects by production La-Cr BiFeO3 perovskite compound annealing at different temperatures i.e., 500 °C, 600 °C, and 700 °C. The photoelectric current and photoelectric polarization were tried to increase with different composition ratios.

Keywords: *Perovskite solar cell, Power conversion efficiency, Annealed La-Cr co-doped BiFeO3, Sol-gel auto-combustion technique.*

1. Introduction

A solar cell, also known as a photovoltaic cell, is a device that uses the photovoltaic effect to directly convert energy into electrical energy. The vast majority of solar cells are made of silicon, which improve the efficiency light and lower the cost of the materials which is progressed from non-crystalline to polycrystalline to single crystal silicon formation. Solar cells, neither fuel cell, do not use chemical changes or dependence upon fuel to generate electricity, and they do not have any moving components, apart from electric generators (Moradnia *et al*., 2020). The crystalline structure known as "Perovskite" was discovered by a Russian physicist named Lev Perovskite. The three components of the construction, which had a cube basis, were designated as ABX3. He discovered the oxide perovskite, that is a well-known crystal and ceramic for researchers and is relatively stable under many conditions.

*Corresponding author's ORCID ID: 0009-0000-2799-682X
DOI: https://doi.org/10.14741/ijcet/v.14.1.1

The 2+ metal charge in the A place, the 4+ metal charge in the B place, and the 2 oxygen ions in the O place make up the oxide perovskite crystal. CaTiO3 and BaTiO3 perovskite Perovskite (ABO3) metal oxides are extensively explored for their promising physical features such as transition superconductivity, photocatalytic activity, optical transparency, nano magnetism, and spin storage. A route for technological applications is particularly found in the interweaving strands between these materials' optical and magnetic characteristics. Wide band gap semiconductors with Curie temperatures (Tc) at or above room temperature (RT) have also been a focus for spintronic applications (Avinash *et al*., 2019).

People are looking for versatile devices in this innovative era of technology that can perform quickly and use little energy. Utilizing the spin and charge of electrons makes it possible to create such intelligent devices. A newer technology called spintronic, commonly referred to as the foundation of magneto-

electronics is the potential utilization of both the spin and charge of electrons.

Future technology can be made from multifunctional multiferroics (MFs), which display several multifunctional features simultaneously. Multifunctional multiferroics (MFs), which 17 simultaneously exhibit many multifunctional properties, can be used to create future technology. Due to their numerous uses in photocatalysis, sensors, as well as spin light emitting diodes, MFs are flexible materials (Mao *et al*., 2019).

2. Methodology

2.1 Material

The sample of analytical grade chemicals using stoichiometric amount of Bi $(NO_3)_3.5H_2O$), La $(NO_3)_3{\cdot}6H_2O$), Fe $(NO_3)_3.9H_2O$, Cr $(NO_3)_3.9H_2O$, citric acid ($C_6H_8O_7.H_2O$) along with ammonia (NH_3) and de-ionized water used to make nanostructure by sol-gel auto-combustion technique. Because of analytical grade elements so there was no need to purify them before using.

2.2 Methods

2.2.1 Sol-gel auto Combustion Method

Inorganic ceramic and composite materials are frequently prepared via sol-gel auto combustion, which has controllable properties for a variety of applications (Deganello & Tyagi, 2018; González-Cortés & Imbert, 2013). This is a unique method that combines the combustion process with the chemical sol-gel process. Sol-gel auto-combustion benefits from low-cost precursors, an easy preparation process, and a powder that is produced that is homogeneous, nanoscale, and highly reactive (Yue, Zhou, Li, Zhang, & Gui, 2000). The sol-gel auto combustion process has therefore been regarded as a desirable and effective method for the synthesis of oxide materials. The samples for the current study were created using the sol-gel method.

The perovskite samples La and Cr doped $BiFeO_3$ employed in this study were created. This technique is based on the exothermic reaction that occurs when aqueous solutions of oxidizers (hydrated metallic nitrates) and organic fuels like citric acid, urea, and ethyl glycol are mixed together. The oxidant and fuel are involved in a redox reaction that is thermally driven. This method produced a homogenous, very reactive, and Nano-sized powder. A single-phase perovskite powder can be produced using standard techniques, but at lower calcination temperatures or in less time. One of the most popular types of solution combustion involves the use of metal nitrates in combination with citric acid as the fuel and the oxidant source. In combustion process, reaction itself provides energy for the reaction of components and there is no need of using high temperature furnace. Metal nitrates and fuel are mixed together to create an aqueous solution in DI water. Then, the solution is heated in order to transform it into a viscous gel. Large-scale gas evolution triggers exothermic self-propagating combustion, which continues until all of the gel has completely burned away. Following initial high-temperature calcination of the yield, fine, pure powder is produced. Therefore, this synthesis approach produced a homogeneous product quickly without the need for a high temperature furnace. The ratio of metal nitrates (oxidant) to fuel (reducing agent) in the auto combustion process is crucial in determining how the reaction will turn out. The ratio of fuel to oxidizer generates a lot of heat throughout the reaction, making it important to manage the reaction's temperature. Due to the sluggish fuel reaction, raw materials do not burn entirely when the fuel to oxidizer ratio is improper, and this causes it to act as a complicated creator (Sytschev & Merzhanov, 2004).

2.2.2 Experimental Procedure

Organic fuel such as citric acids were used as a fuel for the manufacture of La and Cr doped $BiFeO_3$ perovskite material, lanthanum and Cr doped $BiFeO_3$ was used as an oxidant. By stirring, the oxidizer and fuel were individually dissolved in deionized water. Then, while stirring, one solution will be dissolved into another by adding drops at a time. Fuel was introduced after mixing all of the oxidizer solutions, and after a half-hour of continuous stirring, no heat was applied. The solution also included the proper concentrations of ammonia. The pH of the solution mixture was adjusted to 7 using ammonia. After this the homogenous solution heated by hot plate at temperature of 80 °C for one hour with continuous stirring and powder at 300 °C through self-induced combustion mechanism in which fuel present in the precursor solution burns the oxidizer. The resulting ash was grinded to obtain fine powder and placed in a furnace where it was annealed at 500 °C for 3 hours ,600 °C for 3 hours, and 700 °C for 3 hours. After annealing the powder was done in form of characterization.

2.2.3 characterization technique

Infrared spectroscopy and X-ray diffraction was used to determine the structural characteristics of nanostructures (XRD) characterize the produced perovskite, and a scanning electron microscope was used to examine the samples' morphology (SEM). X-ray diffraction patterns was un cover the formation of the perovskite structure in the sample prepared by sol-gel method. The prepared sample characterized by few characterization techniques which was discussed as below.

3. Results and Discussion

3.1 X-ray diffraction

The crystalline phase of the synthesized $Bi_{0.80}La_{0.2}Fe_{0.85}Cr_{0.15}$ materials were examined by X-Ray

Diffraction analysis (XRD). XRD pattern was determined by using a Philips X'pert pro super diffractometer with Cu-Kα radiation of wavelength (λ=1.5418 Å) working at 40 kV voltage, 30 mA current, shown in figure 4.1. Synthesized nanomaterial was sintered at 500°C 600°C 700°C for 3 hours for purity and refinement of crystal structure. XRD peaks of the synthesized BLFCO-1, BLFCO-2, BLFCO-3 were matched with reference JCPDS reference no. 71-2494. The XRD pattern confirmed rhombohedral crystal structure with the help of X' Pert High Score software. Comparison of XRD pattern shows that synthesized electrolyte material has peaks at particular positions.

In order to determine the crystallite size as well as the structure of fabricated specimen, X-ray diffraction spectroscopy is used. Different materials can be used for the emission of X-rays but in current analysis Cu- K alpha radiations having 1.54 nm wavelengths are used. The analyzed peaks confirm the formation of pure crystals of cobalt oxide. A reflection lies in the range of 10° to 80°. The data obtained from XRD analysis give crystallite size, dislocation density, micro-strain and structure (Black *et al.*, 2022).

The XRD method involves directing a beam of X-rays onto a crystalline sample at various angles. The X-rays interact with the crystal lattice and undergo constructive interference, resulting in the generation of diffraction patterns. These patterns contain information about the arrangement of atoms or molecules within the crystal lattice

Through Debye Scherrer's Formula, the micro-strain and size of sub micrometer crystal grains of $Bi_{0.80}La_{0.2}Fe_{0.85}Cr_{0.15}O_3$ composites can be identified.

$$D = \frac{K\lambda}{\beta Cos\theta}$$

D represents the average size of the crystalline domains. K is the shape factor, typically taken as a constant value around 0.9. λ is the wavelength of the X-rays or neutrons used in the diffraction experiment. β is the full width at half maximum (FWHM) of the diffraction peak, measured in radians. θ is the Bragg angle, the angle at which the diffraction peak occurs (Yu *et al.*, 2015).

The Scherrer equation assumes that the broadening of the diffraction peak is primarily due to the finite size of the crystalline domains within the material. It is important to note that this method provides an estimate of the average size of the crystalline domains, and the actual distribution of sizes may be more complex. The Scherrer method is commonly used in materials characterization to obtain information about the crystal size and microstructural properties of powders, thin films, and other crystalline materials.

The crystallographic dislocation density is a manner at which atoms of a crystal sample arranged themselves. In other words it is a structural change due to the transfer of atoms is called dislocation density(Rajendran and Prabha, 2016).

$$\text{Dislocation density} = \frac{1}{(\text{crystlline size})^2}$$

A strain is a response in which the shape, volume or length of material is changed or dislocate when stress apply. The micro strain is denoted by &. For the calculation of micro strain of crystalline materials, the following formula is used (Xu *et al.*, 2021).

$$\text{Strain} = \varepsilon = \frac{\beta cos\theta}{4}$$

The Williamson-Hall method, also known as the Warren-Averbach method, is a technique used to analyze X-ray diffraction data to estimate the average crystallite size and the micro strain present in a crystalline material.

To apply the Williamson-Hall method, you need the full width at half maximum (FWHM) of a diffraction peak from the X-ray diffraction pattern. The FWHM represents the angular width of the peak at half of its maximum intensity.

The Williamson-Hall equation is as follows:

$$\beta\cos\theta = \frac{K\lambda}{(L\cos\theta)} + 4\varepsilon\sin\theta$$

Where:

β is the FWHM of the diffraction peak, θ is the Bragg angle at which the peak occurs,
K is the Scherrer constant (usually taken as 0.9), λ is the wavelength of the X-ray radiation used, L is the average crystallite size, and ε is the micro strain.

To determine the crystallite size and micro strain, you plot βcosθ against 4εsinθ for a series of diffraction peaks. The slope of the resulting linear plot corresponds to 1/L, the inverse of the average crystallite size, and the y-intercept corresponds to 2ε, twice the value of the macrostrain.

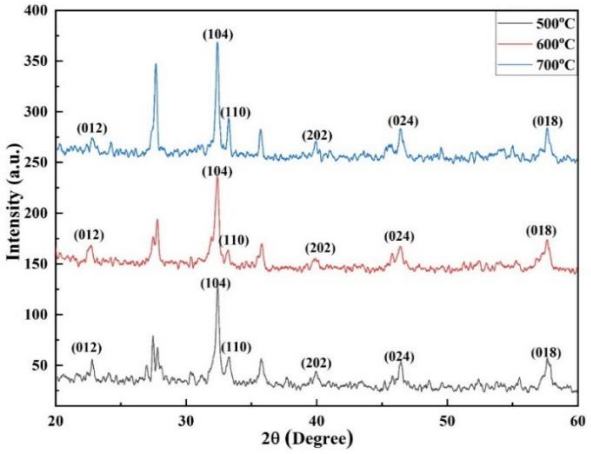

Figure 1: XRD Combined pattern of La/Cr doped with BFO Annealed at 500 °C, 600 °C and 700 °C. $Bi_{0.80}La_{0.2}Fe_{0.85}Cr_{0.15}O_3$ BLFCO-1, BLFCO-2, BLFCO-3.

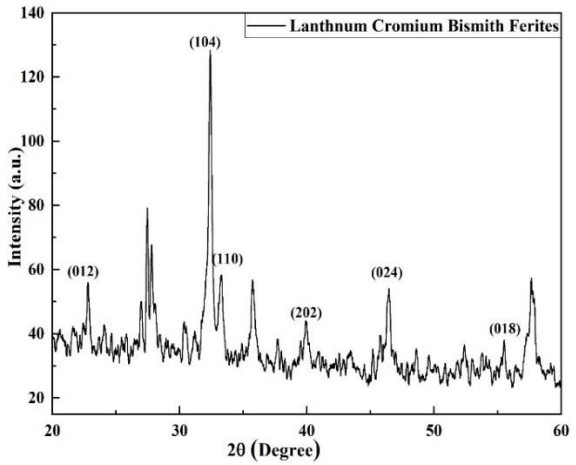

Figure 2: XRD pattern of $Bi_{0.80}La_{0.2}Fe_{0.85}Cr_{0.15}O_3$ Annealed at 500 °C

It is a graph between intensity and angle (2Θ). From above graph we can calculate crystal size of our sample. Following table shows the crystal size of our sample.

a) X-ray diffraction pattern of $Bi_{0.80}La_{0.2}Fe_{0.85}Cr_{0.15}O_3$

The XRD spectrum of $Bi_{0.80}La_{0.2}Fe_{0.85}Cr_{0.15}O_3$ is shown in the fig 1 and explored the peaks at values of 2θ = 22°, 32°, 33°, 39°, 46°and 55°, corresponds to (012), (104), (110), (202), (024), (018), planes respectively depicted in figure 2. The peaks appeared in XRD spectrum were well matched with JCPDS card 71-2494 and structure was rhombohedral. XRD data including crystal size, strain, dislocation density of $Bi_{0.80}La_{0.2}Fe_{0.85}Cr_{0.15}O_3$ are shown in table 1. The measured (hkl) values correspond to the cubic crystal system. The calculated structural parameters are a=5.5759Å α= β=90° γ= 120°. Moreover, at this intensity the crystalline size of $Bi_{0.80}La_{0.2}Fe_{0.85}Cr_{0.15}O_3$ is calculated by Scherer formula 17.47936 nm and average dislocation density was 0.00397941 lines/ m^2.

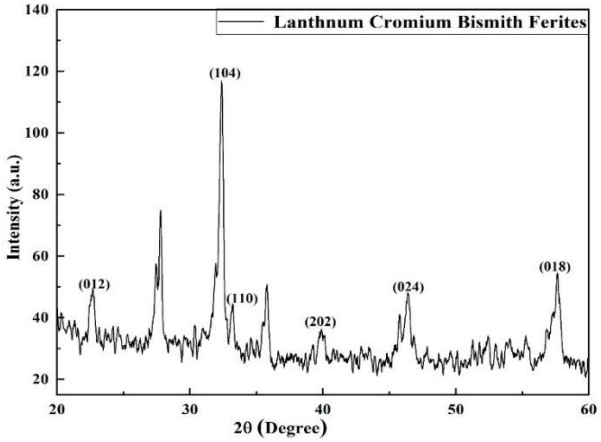

Figure 3: XRD pattern of $Bi_{0.80}La_{0.2}Fe_{0.85}Cr_{0.15}O_3$ Annealed at 600°C

It is a graph between intensity and angle (2Θ). From above graph we can calculate crystal size of our sample. Following table shows the crystal size of our sample.

(b) X-ray diffraction pattern of $Bi_{0.80}La_{0.2}Fe_{0.85}Cr_{0.15}O_3$

The XRD spectrum of $Bi_{0.80}La_{0.2}Fe_{0.85}Cr_{0.15}O_3$ is shown in the fig 3 and observe the peaks at values of 2θ = 22°, 32°, 33°, 39°, 46°and 57°, corresponds to (012), (104), (110), (202), (024), (018), planes respectively shown in figure 3. The peaks appeared in XRD spectrum were well matched with JCPDS card 71-2494 and structure was rhombohedral. XRD data including crystal size, strain, dislocation density of $Bi_{0.80}La_{0.2}Fe_{0.85}Cr_{0.15}O_3$ are shown in table 1. The measured (hkl) values correspond to the cubic crystal system. The calculated structural parameters are a=5.5625Å α= β=90° γ= 120°. Moreover, at this intensity the crystalline size of $Bi_{0.80}La_{0.2}Fe_{0.85}Cr_{0.15}O_3$ is calculated by Scherer formula 13.8003 nm and average dislocation density was 0.00665681 lines/ m^2.

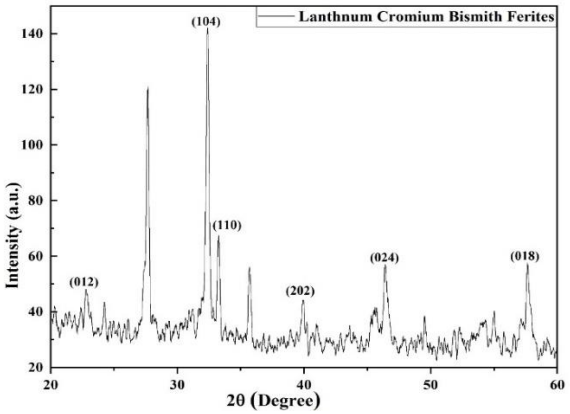

Figure 4: XRD pattern of $Bi_{0.80}La_{0.2}Fe_{0.85}Cr_{0.15}O_3$ Annealed at 700 °C

It is a graph between intensity and angle (2Θ). From above graph we can calculate crystal size of our sample. Following table shows the crystal size of our sample.

(c) X-ray diffraction pattern of $Bi_{0.80}La_{0.2}Fe_{0.85}Cr_{0.15}O_3$

The XRD spectrum of $Bi_{0.80}La_{0.2}Fe_{0.85}Cr_{0.15}O_3$ is shown in the fig 4 and observe the peaks at values of 2θ = 22°, 32°, 33°, 39°, 46°and 57°, corresponds to (012), (104), (110), (202), (024), (018), planes respectively shown in figure 4.4. The peaks appeared in XRD spectrum were well matched with JCPDS card 71-2494 and structure was rhombohedral. XRD data including crystal size, strain, dislocation density of $Bi_{0.80}La_{0.2}Fe_{0.85}Cr_{0.15}O_3$ are shown in table 1. The measured (hkl) values correspond to the cubic crystal system. The calculated structural parameters are a=5.5667Å α= β=90° γ= 120°. Moreover, at this intensity the crystalline size of $Bi_{0.80}La_{0.2}Fe_{0.85}Cr_{0.15}O_3$ is calculated by Scherer formula 11.91286 nm and average dislocation density was 0.00734566 lines/ m^2.

Table 1: Average Crystalline Size, Strain and Average Dislocation Density

Samples	Temperature	Average Crystalline Size	Strain	Average Dislocation Density
BLFCO-1	500 °C	17.47936	0.119797	0.00397941
BLFCO-2	600 °C	13.8003	0.154974	0.00665681
BLFCO-3	700 °C	11.91286	0.167119	0.00734566

3.2. Morphological analysis

The BLFCO samples were studied by SEM to analyses their surface morphology, detect the presence/absence of impurity phases and determine the microstructure parameters. The micro-photographs were presented at different magnifications due to the different grain sizes. Scanning electron microscopy SEM was performed for analysis of morphological properties of synthesized Bi, La, Fe, Cr, SEM of at different magnification range which give us clear images of nanoparticles which shows particles of different sizes in different ranges. Figure 5 shows SEM images of BLFCO-1 nanoparticles at different magnification ranges (X2210, X3547, X8360,) at different resolution(5µm,3µm,1µm). In which SEM micrographs have been used to analyze morphologies of pure and doped BFO NPs that have been calcined at 500 °C. Figure 6 shows chemically synthesized of BLFCO-2 at different magnification ranges (X2197, X3538, and X6894) at different resolution (5µm,3µm,1µm). in which SEM micrographs have been used to analyze morphologies of pure and doped BFO NPs that have been calcined at 600 °C. Figure 7 shows SEM images of BLFCO-3 nanoparticles at different magnification ranges (X2193, X3213, X6263,) at different resolution (5µm,3µm,1µm). in which SEM micrographs have been used to analyze morphologies of pure and doped.

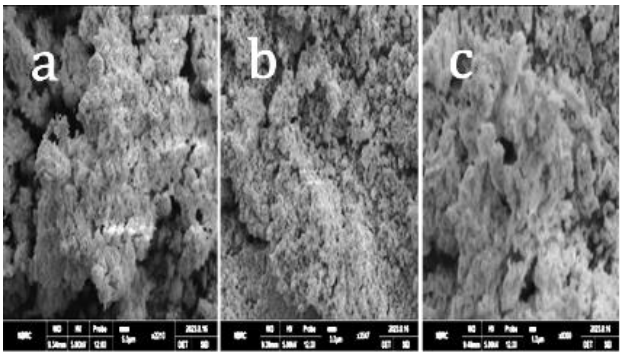

Figure 5: Sample of SEM (BLFCO-1) High resolution SEM micrographs of prepared microstructure of La & Cr doped BFO annealed at 500 °C

The Figure 5 exhibits SEM image of the pure BFO NPs i.e., $Bi_{0.80}La_{0.2}Fe_{0.85}Cr_{0.15}$ O_3 sample of high-resolution magnification using secondary electron image mode for surface and morphological analysis. At this stage, in fig (a) size is magnified up to 2210 times. The indicated scale bar of 5µm gives a sense of the size range of the synthesized microstructures.in fig (b) size is magnified up to 3547 times. The indicated scale bar of 3µm gives a sense of the size range of the synthesized microstructures. in fig (c) size is magnified up to 8360 times. The indicated scale bar of 1µm gives a sense of the size range of the synthesized microstructures. SEM micrographs have been used to analyze morphologies of pure and doped BFO NPs that have been calcined at 500 °C. Additionally, the shapes and sizes of the grains in this location differ and exhibit distinct morphologies. The porosity of the sample, the voids and flaws at the grain boundaries, and the grain sizes and shapes all play a vital influence in determining the sample's many functional qualities.

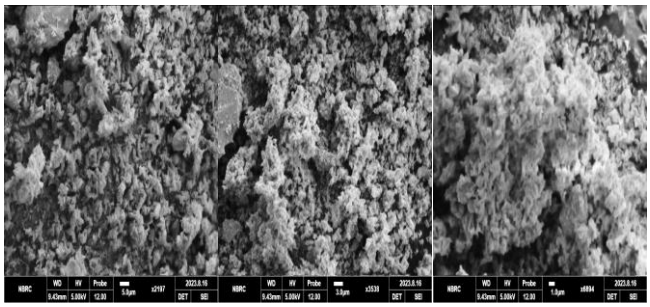

(d) (e) (f)

Figure 6: Sample of SEM (BLFCO-2) High resolution SEM micrographs of prepared microstructure of La & Cr doped BFO annealed at 600 °C**.**

Figure 6 exhibits SEM image of the pure BFO NPs i.e.,of high-resolution magnification using secondary electron image mode for surface and morphological analysis. At this stage, in fig (d) size is magnified up to 2197 times. The indicated scale bar of 5µm gives a sense of the size range of the synthesized microstructures. in fig (e) size is magnified up to 3538 times. The indicated scale bar of 3µm gives a sense of the size range of the synthesized microstructures. in fig (f) size is magnified up to 6894 times.

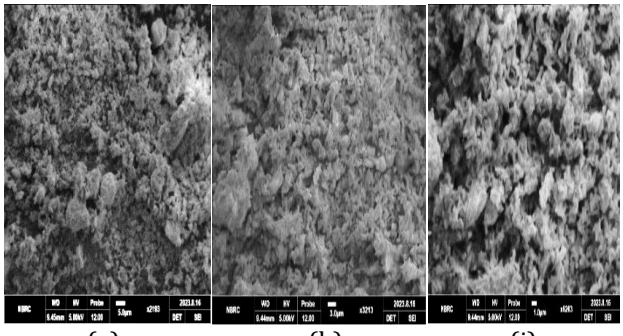

(g) (h) (i)

Figure 7: Sample of SEM (BLFCO-3) High resolution SEM micrographs of prepared microstructure of La & Cr doped BFO annealed at 700 °C

The Figure 7 exhibits SEM image of the pure BFO NPs i.e., Bi0.80La0.2Fe0.85Cr0.15 O3 sample of high-resolution magnification using secondary electron image mode for surface and morphological analysis. At this stage, in fig (g) size is magnified up to 2193 times. The indicated scale bar of 5µm gives a sense of the size range of the synthesized microstructures. in fig (h) size is magnified up to 3213 times. The indicated scale bar of

3µm gives a sense of the size range of the synthesized microstructures. in fig (i) size is magnified up to 6263 times. The indicated scale bar of 1µm gives a sense of the size range of the synthesized microstructures. SEM micrographs have been used to analyze morphologies of pure and doped BFO NPs that have been calcined at 700 °C. Additionally, the shapes and sizes of the grains in this location differ and exhibit distinct morphologies. The porosity of the sample, the voids and flaws at the grain boundaries, and the grain sizes and shapes all play a vital influence in determining the sample's many functional qualities.

3.3 IV Measurements via four-point collinear probe

To investigate current voltage (IV) characteristics of pure $BiFeO_3$ and doped samples i.e., $Bi_{0.80}La_{0.2}Fe_{0.85}Cr_{0.15}O_3$ annealed at 500 °C, $Bi_{0.80}La_{0.2}Fe_{0.85}Cr_{0.15}O_3$ annealed at 600 °C and $Bi_{0.80}La_{0.2}Fe_{0.85}Cr_{0.15}O_3$ annealed at 700 °C with same concentration nanoparticles measurements Keithley 2400 source meter, four-point collinear probe was used. Resistivity test was performed by using pure $BiFeO_3$ and doped form $BiFeO_3$ i.e., $Bi_{0.80}La_{0.2}Fe_{0.85}Cr_{0.15}O_3$, $Bi_{0.80}La_{0.2}Fe_{0.85}Cr_{0.15}O_3$, and $Bi_{0.80}La_{0.2}Fe_{0.85}Cr_{0.15}O_3$ with same concentration. The probes were attached to the pellets via crocodile clips for measuring currents and voltage of required samples. A voltage sweep range of -10V to +10V was set for sample pure BLFCO-1, BLFCO-2, BLFCO-3 and the resulted currents were measured. IV measurements were taken at room temperature. The current voltage measurements were shown in figures below for Sample pure BLFCO-1, BLFCO-2, and BLFCO-3.

The resistivity was calculated via following formulae

$\rho = \pi/\ln 2 \times V/I \times t \times k$

where:

ρ = volume resistivity (Ω-cm)

V = the measured voltage (volts)

I = the source current (amperes)

t = the sample thickness (cm)

k = a correction factor based on the ratio of the probe to wafer diameter and on the ratio of wafer thickness to probe separation

The conductivity was calculated via following formulae:

$\sigma = 1/\rho$

where:

ρ is the resistivity and σ is the conductivity.

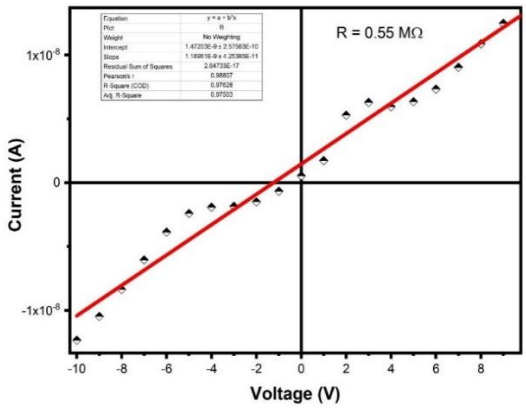

Figure 8: Current voltage plots of IV $Bi_{0.80}La_{0.2}Fe_{0.85}Cr_{0.15}O_3$ BLFCO-1 at 500°C

In figure 8 the current and voltage measurements of doped bismuth ferrite i.e., $Bi_{0.80}La_{0.2}Fe_{0.85}Cr_{0.15}O_3$ were shown. And using the above-mentioned formulae of resistivity, the resistivity was calculated.

For Resistance = 8.40 x 10^9 Ω

$\rho = \frac{\pi}{\ln 2}$ x R x t x k
$\rho = \frac{\pi}{\ln 2}$ x R x 0.0008
ρ = 4.532 x 8.40 x 0.0008 x 10^9
ρ = 0.030455 x 10^9
ρ = 3.045 x 10^7 Ω-cm

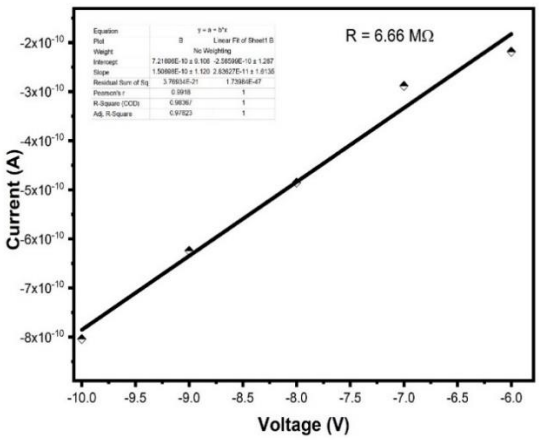

Figure 9: Current voltage plots of IV $Bi_{0.80}La_{0.2}Fe_{0.85}Cr_{0.15}O_3$ BLFCO-2 at 600°C

In figure 9 the current and voltage measurements of doped bismuth ferrite i.e., $Bi_{0.80}La_{0.2}Fe_{0.85}Cr_{0.15}O_3$ were shown. And using the above-mentioned formula of resistivity, the resistivity was calculated.

For Resistance = 6.63 x 10^9 Ω

$\rho = \frac{\pi}{\ln 2}$ x R x t x k
$\rho = \frac{\pi}{\ln 2}$ x R x 0.0008
ρ = 4.532 x 6.63 x 0.0008 x 10^9
ρ = 0.024037 x 10^9
ρ = 2.403 x 10^7 Ω-cm

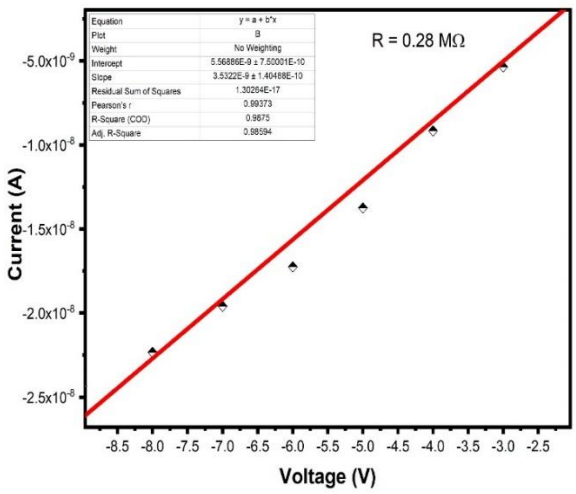

Figure 10: Current voltage plots of IV $Bi_{0.80}La_{0.2}Fe_{0.85}Cr_{0.15}O_3$ BLFCO-3 at 700°C

In figure 10 the current and voltage measurements of doped bismuth ferrite i.e., $Bi_{0.80}La_{0.2}Fe_{0.85}Cr_{0.15}O_3$ were shown. And using the above-mentioned formulae of resistivity, the resistivity was calculated.

For Resistance = 2.83 x 10^9 Ω

$\rho = \frac{\pi}{\ln 2}$ x R x t x k
$\rho = \frac{\pi}{\ln 2}$ x R x 0.0008
ρ = 4.532 x 2.83 x 0.0008 x 10^9
ρ = 0.0102604 x 10^9
ρ = 1.026 x 10^7 Ω-cm

Table 2: Resistivity, Conductivity plots of IV La-Cr doped $BiFeO_3$ sample.

Sample	Temperature	Resistance(Ω)	Resistivity (Ω-cm)	Conductivity
BLFCO-1	500 °C	8.40 x 10^9	3.045 x 10^7	3.28 x 10^{-8}
BLFCO-2	600 °C	6.63 x 10^9	2.403 x 10^7	4.16 x 10^{-8}
BLFCO-3	700 °C	2.83 x 10^9	1.026 x 10^7	9.74 x 10^{-8}

Table 2 Shows that resistivity of BFO sample decreases in sample BLFCO-1, BLFCO-2 and BLFCO-3 as LEDs are introduced which implies that conductivity increases in sample BLFCO-1, BLFCO-2 and BLFCO-3 as LEDs introduced. Since the relationship between conductivity and resistivity is inverse.

3.4 UV-Visible spectroscopy

UV-visible spectroscopy is a technique used to analyze the absorption, transmission, and reflection of ultraviolet (UV) and visible light by a substance. It provides information about the electronic structure of molecules and is widely used in various fields, including chemistry, biochemistry, materials science, and environmental science. UV-visible spectroscopy involves passing a beam of light with a range of wavelengths through a sample and measuring the intensity of the light before and after it interacts with the sample. The sample can be a gas, liquid, or solid, and it may be in solution or in a solid-state form. The absorption spectra of the pure and doped samples in the range of 200-800 nm were recorded using a double beam UV-Visible Spectrophotometer. The formula for absorption in the UV-visible region is given by the Beer-Lambert Law, also known as the Beer-Lambert-Bouguer Law. It relates the absorption of light to the concentration of the absorbing species and the path length of the light through the sample. The formula is as follows:

$A = \varepsilon * c * l$

Where A is the absorbance of the sample, ε (epsilon) is the molar absorptivity or molar extinction coefficient, which is a constant specific to the absorbing species and the wavelength of light being used. It represents how strongly the species absorbs light at a particular wavelength, c is the concentration of the absorbing species in mol/L, l is the path length of the light through the sample in centimeters.

The absorbance (A) is related to the transmittance (T) of the sample by the following equation:

$A = -\log(T)$

The Beer-Lambert Law is widely used in UV-visible spectroscopy to quantify the concentration of an absorbing species in a sample based on its absorbance at a specific wavelength.

The energy band gap Eg was measured by using the absorption coefficient (a) from the following equation

$Ahv = B(h-Eg)^n$

Where h is the Planck's constant, v is the frequency of the incident light, B is a constant ratio to material.

UV Visible spectroscopy is a tool used to identify the optical properties of semiconductor nanoparticles. Absorbance depends upon crystal size and the nature of the substituted materials. UV Visible spectroscopy studied the optical characteristics of figure 11 (BLFCO-1) $Bi_{0.80}La_{0.2}Fe_{0.85}Cr_{0.15}$ O_3 at when it is sinter 500 °C shows energy band gap 2.72 eV, figure 12 (BLFCO-2) $Bi_{0.80}La_{0.2}Fe_{0.85}Cr_{0.15}$ O_3 at when it is sinter 600 °C shows energy band gap 2.53 eV and figure 13 (BLFCO-3) $Bi_{0.80}La_{0.2}Fe_{0.85}Cr_{0.15}$ O_3 at when it is sinter 700 °C shows energy band gap 2.42 eV.

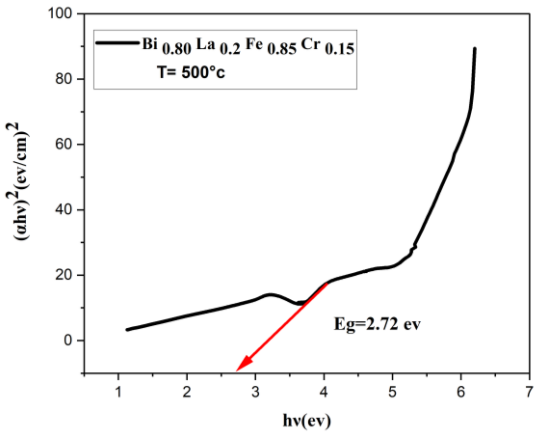

Figure 11: UV graph of BLFCO-1

Fig 11 shows $Bi_{0.80}La_{0.2}Fe_{0.85}Cr_{0.15}O_3$ at when it is sinter 500 °C shows energy band gap 2.72 eV. Optical absorption spectrum of sample $Bi_{0.80}La_{0.2}Fe_{0.85}Cr_{0.15}O_3$ shows a strong and prominent absorption peak and sintered at 500 °C for the pure sample, the band gap is 2.72 eV, doped sample for the concentration $Bi_{0.80}La_{0.2}Fe_{0.85}Cr_{0.15}O_3$. The band gap E_g of the generated samples is also calculated where E_g is a separation between the valence band and conduction band. The given sample absorbs energy because it is moved into a higher energy band. It is also confirmed that materials are insulators, conductors, and semiconductors by the separation of the valence band.

Fig 12 shows $Bi_{0.80}La_{0.2}Fe_{0.85}Cr_{0.15}O_3$ at when it is sinter 600 °C shows energy band gap 2.53 eV. Optical absorption spectrum of sample $Bi_{0.80}La_{0.2}Fe_{0.85}Cr_{0.15}O_3$ shows a strong and prominent absorption peak and sintered at 600 °C for the pure sample, the band gap is 2.53 eV, doped sample for the concentration $Bi_{0.80}La_{0.2}Fe_{0.85}Cr_{0.15}O_3$. The band gap E_g of the generated samples is also calculated where E_g is a separation between the valence band and conduction band. The given sample absorbs energy because it is moved into a higher energy band. It is also confirmed that materials are insulators, conductors, and semiconductors by the separation of the valence band and conduction band.

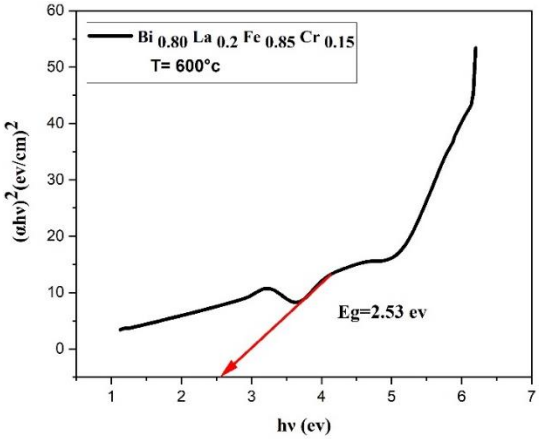

Figure 12: UV graph of BLFCO-2

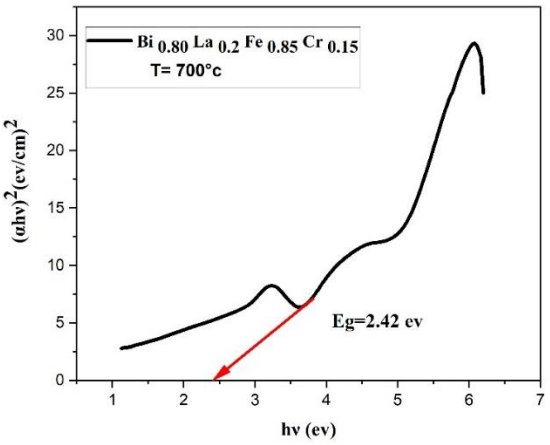

Figure 13: UV graph of BLFCO-3

Fig 13 shows $Bi_{0.80}La_{0.2}Fe_{0.85}Cr_{0.15}O_3$ at when it is sinter 700 °C shows energy band gap 2.42 ev.

In Figure 13 optical absorption spectrum of sample $Bi_{0.80}La_{0.2}Fe_{0.85}Cr_{0.15}O_3$ shows a strong and prominent absorption peak at and sintered at 700 °C for the pure sample, the band gap is 2.42 eV, doped sample for the concentration $Bi_{0.80}La_{0.2}Fe_{0.85}Cr_{0.15}O_3$. The band gap Eg of the generated samples is also calculated where Eg is a separation between the valence band and conduction band. The given sample absorbs energy because it is moved into a higher energy band. It is also confirmed that materials are insulators, conductors, and semiconductors by the separation of the valence band and conduction band.

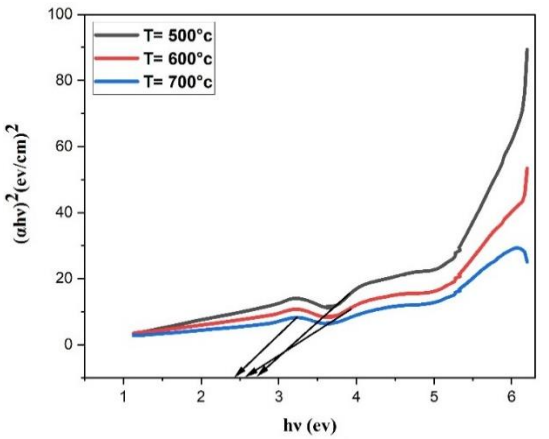

Figure 14: UV Combined graph of BLFCO-1, BLFCO-2 and BLFCO-3 Annealed at 500 °C, 600 °C and 700 °C

UV combined graph shows that how annealing temperature effect the optical energy band gap. When we sinter the sample BLFCO-1 at 500 °C, BLFCO-2 600 °C and BLFCO-3 at 700 °C the energy band ga is 2.72ev, 2.53ev, 2.42ev. The energy band gap decreases at different annealing temperatures the material shows conducting behavior.

Conclusions

Perovskite materials proven themselves as an emerging form of nanomaterials, which are playing a vital role in

the field of energy sector. These materials attain significant attention due to their unique characteristics of an optimum low band gap, good thermal stability, marvelous power conversion efficiency, and economic cost. In this study, Bi0.80La0.2Cr0.15Fe0.85O3 Sol-gel auto-combustion was effectively used to create perovskite after calcined at 500°C 600°C 700°C for 3 hrs. Citric acid was used in the desired sample for gel-formation. Crystal structure, surface morphology, composition, optical band gap, elemental analysis and electrical properties of prepared samples were investigated by XRD, SEM, UV, and IV four probe method respectively. XRD spectra depicts structure of BFO is rhombohedral with space group R3c.

The values of lattice parameters and crystallite size of the prepared sample were observed. The single-phase rhombohedral structure was obtained by diffraction angles 2θ = 22o, 32o, 33o, 39o, 46o, 55o corresponds to (012), (104), (110), (202), (024), (018) planes respectively. Using SEM, it is confirmed that Bi0.80La0.2Cr0.15Fe0.85O3 has agglomerated form nano particles and cloudy have smooth surface having irregular shape and nonuniform distribution. Sample of (Bi0.80La0.2Cr0.15Fe0.85O3) BLFCO-1, BLFCO-2, BLFCO-3 at different magnification range which give us clear images of nanoparticles which shows particles of different size in different range. SEM images of BLFCO-1 nanoparticles at different magnification ranges (X2210, X3547, X8360,) at different resolution(5µm,3µm,1µm) that have been calcined at 500 °C. SEM images of BLFCO-2 at different magnification ranges (X2197, X3538, and X6894) at different resolution (5µm,3µm,1µm) that have been calcined at 600 °C. SEM images of BLFCO-3 nanoparticles at different magnification ranges (X2193, X3213, X6263,) at different resolution (5µm,3µm,1µm) that have been calcined 700 °C. The energy band gap was observed by UV- visible spectroscopy.

From the UV analysis it is observed that optical band gap (Eg) decreased by doping of La and Cr. Band gap of sample BLFCO-1 is 2.73 eV, sintered 500 °C. Band gap of sample BLFCO-2 is 2.52 eV, sintered 600 °C. Band gap of sample BLFCO-3 is 2.42 eV sintered 700 °C. IV analysis is very important about the composition of the prepared materials, from this technique, it is confirmed that there was not any impurity in the prepared samples. Moreover, from the exploration of electrical properties, it was observed that the resistivity decreases and also, it was confirmed that the conductivity increases with the co-doping in the BFO. The resistivity of sample BLFCO-1, BLFCO-2 and BLFCO-3 is 3.045 x 107 Ω-cm, 2.403 x 107 Ω-cm and 1.026 x 107 Ω-cm. The conductivity of sample BLFCO-1, BLFCO-2 and BLFCO-3 is 3.28 x 10-8, 4.16 x 10-8 and 9.74 x 10-8.

References

[1] V., M., & Shagalina O.V. Scientific Supervisor – Associate professor Shagalina O.V. (n.d.). 0960327115603588 (1).

[2] Abdel-Latif, I. A., Ismail, A. A., Faisal, M., Ali, A. M., Al-Salmi, A. E., & Al-Hajry, A. (2017). Impact of the annealing temperature on perovskite strontium doped neodymium manganites nanocomposites and their photocatalytic performances. Journal of the Taiwan Institute of Chemical Engineers, 75, 174–182.

[3] Aghav, P., Dhage, V. N., Mane, M. L., Shengule, D., Dorik, R., & Jadhav, K. (2011). Effect of aluminum substitution on the structural and magnetic properties of cobalt ferrite synthesized by sol–gel auto combustion process. Physica B: Condensed Matter, 406(23), 4350-4354

[4] Afzal, A. M., Javed, Y., Hussain, S., Ali, A., Yaqoob, M. Z., & Mumtaz, S. (2020). Enhancement in photovoltaic properties of bismuth ferrite/zinc oxide heterostructure solar cell device with graphene/indium tin oxide hybrid electrodes. Ceramics International, 46(7), 9161–9169.

[5] Akhtar, M., Saba, S., Arif, S., Mustafa, G. M., Khalid, A., Ali, G., & Atiq, S. (2021). Efficient magnetoelectric dispersion in Ni and Co co-doped BiFeO3 multiferroics. Physica B: Condensed Matter, 602.

[6] Amin, M., Rafique, H. M., Mustafa, G. M., Mahmood, A., Ramay, S. M., Atiq, S., & Ali, S. M. (2021). Effect of La/Cr co-doping on dielectric dispersion of phase pure BiFeO3 nanoparticles for high frequency applications. Journal of Materials Research and Technology, 13, 1534–1545.

[7] Arya, G., Kumar, A., Ram, M., & Singh Negi, N. (N.D.). Structural, dielectric, ferroelectric and magnetic properties of mn-doped bifeo3 nanoparticles synthesized by sol-gel method. International Journal of Advances in Engineering & Technology, 5(2), 245–252.

[8] Attiq-ur-rehman, Ashraf, M. W., Mahmood, A., Rehman, A. ur, Ramay, S. M., & Saleem, M. (2021). Growth of Zr–BiFeO3 nanostructures on two step anodized porous alumina for estimation of optical and dielectric response. Physica E: Low-Dimensional Systems and Nanostructures, 127.

[9] Avinash, M., Muralidharan, M., & Sivaji, K. (2019). Structural, optical and magnetic behaviour of Cr doped BaSnO3 perovskite nanostructures. Physica B: Condensed Matter, 570, 157–165.

[10] Akinwumi, A. O., Rennie, A. R., & Jayawardena, K. D. G. I. (2021). Nanoscience and Nanotechnology: Advances and Applications. Frontiers in Nanotechnology, 3, 30. https://doi.org/10.3389/fnano.2021.654675

[11] Babu, V. J., Vempati, S., Uyar, T., & Ramakrishna, S. (2015). Review of one-dimensional and two-dimensional nanostructured materials for hydrogen generation. Physical Chemistry Chemical Physics, 17(5), 2960-2986.

[12] Basiri, M., Shokrollahi, H., & Isapour, G. (2014). Effects of La content on the magnetic, electric and structural properties of BiFeO3. Journal of Magnetism and Magnetic Materials, 354, 184-189.

[13] Bhattacharya, P., & Gupta, R. K. (2017). Nanotechnology in water and wastewater treatment: Applications and implications. Environmental Chemistry Letters, 15(4), 591-605.

[14] Bréchignac, C., P. Houdy and M. Lahmani. 2008. Nanomaterials and nanochemistry. Springer Science & Business Media.

[15] Chauhan, S., Kumar, M., Yousuf, A., Rathi, P., Sahni, M., & Singh, S. (2021). Effect of Na/Co co-substituted on structural, magnetic, optical and photocatalytic properties of BiFeO3 nanoparticles. Materials Chemistry and Physics, 263.

[16] Chandamma, N., Manohara, B., Ujjinappa, B., Shankarmurthy, G., & Kumar, M. S. (2017). Structural and electrical properties of Zinc doped Nickel ferrites nanoparticles prepared via facile combustion technique. Journal of alloys and compounds, 702, 479-488.

[17] Chen, C., Cheng, J., Yu, S., Che, L., & Meng, Z. (2006). Hydrothermal synthesis of perovskite bismuth ferrite crystallites. Journal of Crystal Growth, 291(1), 135–139.

[18] Chen, G., Chen, J., Pei, W., Lu, Y., Zhang, Q., Zhang, Q., & He, Y. (2019). Bismuth ferrite materials for solar cells: Current status and prospects. In Materials Research Bulletin (Vol. 110, pp. 39–49). Elsevier Ltd.

[19] Dong, G., Fan, H., Tian, H., Fang, J., & Li, Q. (2015). Gas-sensing and electrical properties of perovskite structure p-type barium-substituted bismuth ferrite. RSC Advances, 5(38), 29618–29623.

[20] Deganello, F., & Tyagi, A. K. (2018). Solution combustion synthesis, energy and environment: Best parameters for better materials. Progress in crystal growth and characterization of materials, 64(2), 23-61.

[21] Daniel, M.-C., & Astruc, D. (2004). Gold nanoparticles: assembly, supramolecular chemistry, quantum-size-related properties, and applications toward biology, catalysis, and nanotechnology. Chemical reviews, 104(1), 293-346.

[22] Epp, J. (2016). X-Ray Diffraction (XRD) Techniques for Materials Characterization. In Materials Characterization Using Nondestructive Evaluation (NDE) Methods (pp. 81–124). Elsevier Inc.

[23] González-Cortés, S. L., & Imbert, F. E. (2013). Fundamentals, properties and applications of solid catalysts prepared by solution combustion synthesis (SCS). Applied Catalysis A: General, 452, 117-131.

[24] Glezer, A. (2011). Structural classification of nanomaterials. Russian Metallurgy (Metally), 2011(4), 263.

[25] Haider, S., Liaquat, A., Awan, M. S., Ul-Haq, N., & Ul Haq, & A. (n.d.). Electrical and magnetic properties of BiFeO 3 nanoparticles substituted with high concentrations of cobalt.

[26] Hulla, J. E., Sahu, S. C., & Hayes, A. W. (2015a). Nanotechnology: History and future. In Human and Experimental Toxicology (Vol. 34, Issue 12, pp. 1318–1321). SAGE Publications Ltd.

[27] Hulla, J. E., Sahu, S. C., & Hayes, A. W. (2015b). Nanotechnology: History and future. Human and Experimental Toxicology, 34(12), 1318–1321.

[28] John, J., Suresh, S., Pillai.S, S., Philip, R., & Pillai, V. P. M. (2021). Effect of Fe doping on the structural, morphological, optical, magnetic and dielectric properties of BaSnO3. Journal of Materials Science: Materials in Electronics, 32(9), 11763–11780.

[29] Jalil, A. (2017). Investigation of structural, magnetic and photocatalytic properties of Gd doped bismuth ferrite-reduced graphene oxide nanocomposites.

[30] Kakade, S. G., Ma, Y.-R., Devan, R. S., Kolekar, Y. D., & Ramana, C. V. (2016). Dielectric, complex impedance, and electrical transport properties of erbium (Er3+) ion-substituted nanocrystalline, cobalt-rich ferrite (Co1. 1Fe1. 9–x Er x O4). The journal of physical Chemistry C, 120(10), 5682-5693.

[31] Kim, J. Y., Lee, J. W., Jung, H. S., Shin, H., & Park, N. G. (2020). High-Efficiency Perovskite Solar Cells. In Chemical Reviews (Vol. 120, Issue 15, pp. 7867–7918). American Chemical Society.

[32] Kumari, K., Chakrabarti, T., Jana, A., Bhattachartjee, D., Gupta, B., & Sarkar, S. K. (2018). Comparative Study on Perovskite Solar Cells based on Titanium, Nickel and Cadmium doped BiFeO3 active material. Optical Materials, 84, 681–688.

[33] Li, X. Y., Dai, J. Q., Cao, T. F., & Wang, X. W. (2019). Structure and physical properties of (Zn, Ti) co-doped BiFeO3 ceramics prepared using three different processes. Ceramics International, 45(4), 5015–5022.

[34] Liu, J., Yang, H., & Shen, P. K. (2015). Nanostructured materials for renewable energy conversion and storage devices. Advanced Energy Materials, 5(15), 1500110.

[35] Lu, X., Wang, C., & Wei, Y. (2009). One-dimensional composite nanomaterials: synthesis by electrospinning and their applications. small, 5(21), 2349-2370.

[36] Lin, P., Moore, D., & Allhoff, F. (2009). What is nanotechnology and why does it matter?: from science to ethics: John Wiley & Sons.

[37] Liu, M., & Sun, N. X. (2014). Voltage control of magnetism in multiferroic heterostructures. Philosophical Transactions of the Royal Society A: Mathematical, Physical and Engineering Sciences, 372(2009), 20120439.

[38] Li, M., Ning, M., Ma, Y., Wu, Q., & Ong, C. (2007). Room temperature ferroelectric, ferromagnetic and magnetoelectric properties of Ba-doped BiFeO3 thin films. Journal of Physics D: Applied Physics, 40(6), 1603.

[39] Lee, C. C., MacKay, J. A., Fréchet, J. M., & Szoka, F. C. (2005). Designing dendrimers for biological applications. Nature biotechnology, 23(12), 1517.

[40] Mao, W., Yao, Q., Fan, Y., Wang, Y., Wang, X., Pu, Y., & Li, X. a. (2019). Combined experimental and theoretical investigation on modulation of multiferroic properties in BiFeO3 ceramics induced by Dy and transition metals co-doping. Journal of alloys and compounds, 784, 117-124.

[41] Mieszawska, A. J., Mulder, W. J., Fayad, Z. A., & Cormode, D. P. (2013). Multifunctional gold nanoparticles for diagnosis and therapy of disease. Molecular Pharmaceutics, 10(3), 831-847.

[42] Nadeem, M., Khan, W., Khan, S., Husain, S., Singh, F., Ansari, A., Shukla, D. K., Ahad, A., Chakradhary, V. K., & Akhtar, M. J. (2020). Structural, optical and enhanced multiferroic properties of La/Cr co-substituted BiFeO3 nanostructures. Journal of Materials Science: Materials in Electronics, 31(14), 11177–11194.

[43] Porter, A. L., & Youtie, J. (2009). How interdisciplinary is nanotechnology? In Journal of Nanoparticle Research (Vol. 11, Issue 5, pp. 1023–1041).

[44] Poole Jr, C. P., & Owens, F. J. (2003). Introduction to nanotechnology: John Wiley & Sons.

[45] Perevoshchikova, I., Zorov, D., & Antonenko, Y. (2008). Peak intensity analysis as a method for estimation of fluorescent probe binding to artificial and natural nanoparticles: tetramethylrhodamine uptake by isolated mitochondria. Biochimica et Biophysica Acta (BBA)-Biomembranes, 1778(10), 2182-2190.

[46] Shami, M. Y., Awan, M. S., & Anis-Ur-Rehman, M. (2011). Phase pure synthesis of BiFeO3 nanopowders using diverse precursor via co-precipitation method. Journal of Alloys and Compounds, 509(41), 10139–10144.

[47] Sharma, S., Siqueiros, J. M., & Herrera, O. R. (2021). Structural, dielectric, ferroelectric and optical properties of Er doped BiFeO3 nanoparticles. Journal of Alloys and Compounds, 853.

[48] Shinjo, Y., Mori, M., Fujihara, S., & Hagiwara, M. (2022). Ti doping and low-temperature sintering of BiFeO3 nanoparticles synthesized by the solvothermal method. Ceramics International, 48(22), 32723–32729.

[49] Singh, J. P., Bansal, N. P., American Ceramic Society. Meeting (105th : 2003 : Nashville, Tenn.), International Symposium on Innovative Processing and Synthesis of Ceramics, G., & Ceramic-Matrix Composites Symposium (2003 : Nashville, Tenn.).

[50] Stojadinović, B., Dohčević-Mitrović, Z., Stepanenko, D., Rosić, M., Petronijević, I., Tasić, N., Ilić, N., Matović, B., & Stojanović, B. (2017). Dielectric and ferroelectric properties of Ho-doped BiFeO3 nanopowders across the structural phase transition. Ceramics International, 43(18), 16531–16538.

[51] Stone, V., Nowack, B., Baun, A., van den Brink, N., von der Kammer, F., Dusinska, M., . . . Joner, E. (2010). Nanomaterials for environmental studies: classification, reference material issues, and strategies for physico-chemical characterisation. Science of the total environment, 408(7), 1745-1754.

[52] Shima, H., Naganuma, H., & Okamura, S. (2013). Optical properties of multiferroic BiFeO3 films. Materials Science-Advanced Topics, 33-61.

[53] Sudha, P. N., Sangeetha, K., Vijayalakshmi, K., & Barhoum, A. (2018). Nanomaterials history, classification, unique properties, production and market. In Emerging Applications of Nanoparticles and Architectural Nanostructures: Current Prospects and Future Trends (pp. 341–384). Elsevier Inc.

[54] Sytschev, A. E., & Merzhanov, A. G. (2004). Self-propagating high-temperature synthesis of nanomaterials. Russian chemical reviews, 73(2), 147-159.

[55] Wang, N., Luo, X., Han, L., Zhang, Z., Zhang, R., Olin, H., & Yang, Y. J. N.-M. L. (2020). Structure, performance, and application of BiFeO3 nanomaterials. 12(1), 1-23.

[56] Wei, K., Faraj, Y., Yao, G., Xie, R., & Lai, B. (2021). Strategies for improving perovskite photocatalysts reactivity for organic pollutants degradation: A review on recent progress. In Chemical Engineering Journal (Vol. 414). Elsevier B.V.

[57] Wu, Z. S., Winter, A., Chen, L., Sun, Y., Turchanin, A., Feng, X., & Müllen, K. (2012). Three-dimensional nitrogen and boron co-doped graphene for high-performance all-solid-state supercapacitors. Advanced materials, 24(37), 5130-5135.

[58] Yan, H., Deng, H., Ding, N., He, J., Peng, L., Sun, L., Yang, P., & Chu, J. (2013). Influence of transition elements doping on structural, optical and magnetic properties of BiFeO3 films fabricated by magnetron sputtering. Materials Letters, 111, 123–125.

[59] Yue, Z., Zhou, J., Li, L., Zhang, H., Gui, Z. J. J. o. M., & materials, m. (2000). Synthesis of nanocrystalline NiCuZn ferrite powders by sol–gel auto-combustion method. 208(1-2), 55-60.

[60] Yang, S., Seidel, J., Byrnes, S., Shafer, P., Yang, C.-H., Rossell, M., . . . Ager, J. J. N. n. (2010). Above-bandgap voltages from ferroelectric photovoltaic devices. 5(2), 143-147.